J Mater Sci (2025) 60:5019–5034

Carbonates stabilize interstratified α/β intermediates in the preparation of nickel hydroxide

P. H. Ho[1,2], I. Z. Awan[1,3,4], N. Tanchoux[1], R. Arletti[5], S. Albonetti[3,6], F. Cavani[3,6], A. Martucci[7], H. Petitjean[1], D. Tichit[1], P. Benito[3,6], and F. Di Renzo[1,*]

[1] *ICGM, Université de Montpellier-CNRS-ENSCM, Montpellier, France*
[2] *Institute for Sustainable Hydrogen Economy, Forschungszentrum Jülich, Am Brainenergy Park 4, 52428 Jülich, Germany*
[3] *Department Industrial Chemistry "Toso Montanari", Alma Mater Studiorum Università di Bologna, Bologna, Italy*
[4] *Department Chemistry, Lahore Garrison University, Lahore, Pakistan*
[5] *Department Chemical and Geological Sciences, University of Modena and Reggio Emilia, Modena, Italy*
[6] *C3 Center for Chemical Catalysis, Alma Mater Studiorum, Alma Mater Studiorum Università di Bologna, Bologna, Italy*
[7] *Department Physics and Earth Sciences, University of Ferrara, Ferrara, Italy*

Received: 28 May 2024
Accepted: 14 February 2025
Published online: 11 March 2025

ABSTRACT

The phases formed by alkaline precipitation of $Ni(OH)_2$ at different temperatures and different levels of carbonate and nitrate anions have been characterized by X-ray diffraction, elemental analysis, FTIR spectroscopy, TG-MS, N_2 physisorption and cyclic voltammetry. The dehydration-deanionization of α- to β-$Ni(OH)_2$ passes through an interstratified intermediate IS-$Ni(OH)_2$, which can be stabilized at 80 °C in the presence of carbonates. IS-$Ni(OH)_2$ materials have been prepared with CO_3^{2-}/Ni^{2+} ratio ranging from 0.05 to 0.16, resulting in different ratios of interstratified α and β phase layers. IS-$Ni(OH)_2$, thermally stable up to 200 °C, presents a peculiar ink-bottle mesoporosity and surface area higher than 100 $m^2\ g^{-1}$. The material is promising for electrocatalytic applications on the basis of the textural properties and a reproducible reduction potential of 0.37 V versus SCE. The easily reversible reducibility of Ni^{2+} is also shown by the TG-MS of the thermal dehydroxylation-deanionization to NiO, evidencing transient Ni^{3+} species formed by reaction with NO_x emitted from the decomposition of nitrates.

Handling Editor: Andréa de Camargo.

Address correspondence to E-mail: francesco.di-renzo@umontpellier.fr

https://doi.org/10.1007/s10853-025-10735-7

GRAPHICAL ABSTRACT

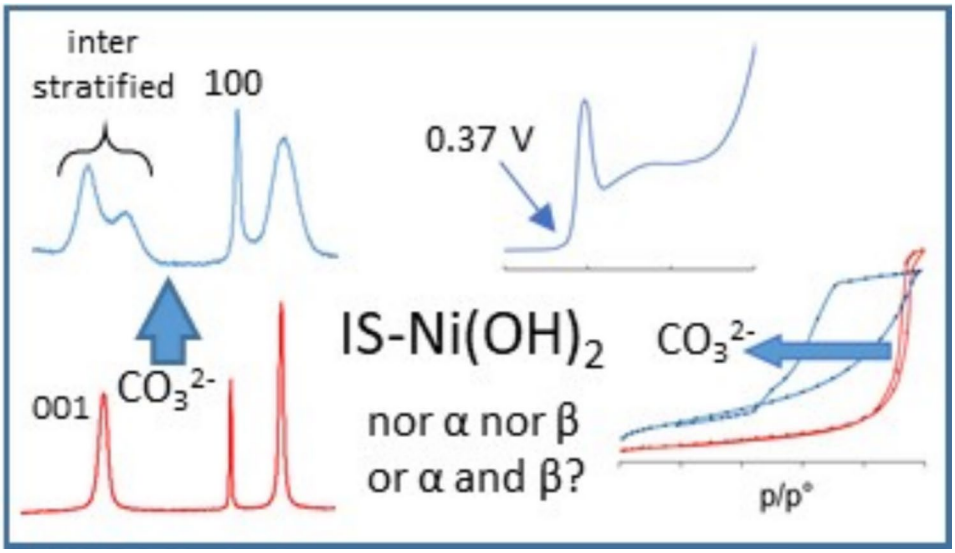

Introduction

Nickel hydroxide has been the forerunner of the nickel cathodes for rechargeable batteries. The reproducibility of its Ni^{2+}/Ni^{3+} redox cycle has allowed the introduction of some of the earliest industrially viable alkaline batteries: the Ni–Cd batteries of Jungner in 1899, now gradually discarded by environmental concern, and the Ni–Fe batteries of Edison in 1901, still used in some heavy-duty installations [1]. Today, nickel hydroxide is an important component of the cathode for nickel-metal hydride batteries for portable devices and consumer goods [2–4] and of the electrodes for several types of Li-ion batteries for electric vehicles [5, 6]. $Ni(OH)_2$ is also used in water electrolyzers [7–9], sensing electrocatalysts [10], and oxidation photocatalysts [11].

Two main phases of Ni^{2+} hydroxides have been defined: an anhydrous β-$Ni(OH)_2$ phase, corresponding to the mineral theophrastite, with a brucite-like structure formed by stacked hydrogen-bonded layers of edge-sharing $Ni(OH)_6$ octahedra [12], and a hydrated α-$Ni(OH)_2$ phase, a swollen brucite structure with intercalated water and anions that induce a turbostratic orientational disorder in the stacking of the layers [13]. $Ni(OH)_2$ is prepared either by electrochemical deposition or by precipitation of Ni^{2+} salts in alkaline, ammonia or urea solutions [14]. α-$Ni(OH)_2$ prepared in the presence of anions was early shown to be a hydroxysalt, with a significant retention of the anions of the parent salt in the interlayer [14–19]. β-$Ni(OH)_2$ can be formed by dehydration-deanionization of α-$Ni(OH)_2$ aging in solution [14, 20, 21]. The temperature of the aging treatment has been classically shown to kinetically favor the α-to-β transformation of $Ni(OH)_2$ [14, 20], albeit the transition also occurs at room temperature by osmotic exchange with the surrounding solution [22, 23].

The configuration of anions in the expanded brucite-like structure of α-$Ni(OH)_2$ has been the object of extended debate in the literature [24], as it proposes an interesting charge-compensation conundrum. Several structural hypotheses have been formulated to explain the compensation of the anion charge in a brucite-like structure with divalent cations $Ni^{2+}(OH)_2{\cdot}nH_2O$ that, as such, is itself charge-compensating and does not present a positive charge able to compensate additional anions [24–26]. Classically, additional positive charge could be provided by trivalent cations replacing a fraction of Ni^{2+} in the brucite layer, with the well-known charge-compensation mechanism of hydrotalcite-like layered double hydroxides (LDH) $M^{2+}{}_{3-x}M^{3+}{}_x(OH)_6A_x$, where the charge of the anion A compensates the charge of a trivalent cation in the layer of divalent-centered octahedra. This mechanism has been observed in the case of the replacement of a fraction of Ni^{2+} by Co^{3+}, Fe^{3+} or Mn^{4+} in α-$Ni(OH)_2$ [27–30]. Also Ni^{3+} has been considered as a possible

trivalent cation but the presence of Ni^{3+} has been generally discarded on the basis of the green color of the precipitates, typical of Ni^{2+} and well different from the black color of Ni^{3+}-bearing materials [16, 17].

In the absence of an additional cation charge, the charge of the anions is likely compensated by their direct connection with the brucite-like layers. Grafting of the anion to the layer, with substitution of a hydroxy group by the oxygen of the anion, can result in a charge-neutral layered hydroxysalt. This configuration has been often proposed for anions in nickel hydroxides [18, 25, 26, 31] and has been corroborated by DFT modeling of nitrates in α-$Ni(OH)_2$ [32]. Sharing oxygen between metal and anions is encountered in the structure of several hydroxysalts, like $Cu_2(OH)_3NO_3$, orthorhombic gerhardtite or monoclinic rouaite [33, 34], and $Zn_3(OH)_4(NO_3)_2$ [35]. It is interesting to observe that basic synthesis conditions are critical for forming brucite-like structures with bound anions. In different synthesis conditions, the higher divalent/OH ratio brings to the formation of nickel vacancies [19]. At high divalent/OH ratios, the brucite layer can be disrupted. For instance, $Zn(OH)(NO_3).H_2O$ is formed by parallel double chains of octahedra, each Zn^{2+} being bonded to two hydroxyls, two nitrate anions and two water molecules [36]. $Ni_3(OH)_2(SO_4)_2(H_2O)_2$ presents criss-crossing chains of Ni^{2+} octahedra, linked by sulfate anions in an antlerite-like material [37]. $Ni_2CO_3(OH)_2$ and $Co_2CO_3(OH)_2$ materials, with rosasite or malachite structures, feature puckered layers of octahedra connected by bridging carbonates [38–40].

A better understanding of the role of anions in the formation of $Ni(OH)_2$ phases is relevant in the present context of rising interest for the applications of layered hydroxysalts as intercalation compounds [24, 41, 42]. The role of interlayer anions has been highlighted in the elaboration of (Co, Ni)$(OH)_2$ materials as supercapacitors for energy storage [43–46] and is also relevant for the recovery of nickel in hydrometallurgical treatment of nickel ore [47–49], in the recycling of wastes from metal plating or batteries [50, 51] or in metallurgical precursors of structured NiO [52].

The level of anion incorporation is at the basis of the formation of IS-$Ni(OH)_2$, a material which has early been defined as a "nickel hydroxide phase which is neither α nor β" [53]. This material is defined by its XRD pattern, which is typical of random interstratification of brucite-like layers. When $Ni(OH)_2$ layers are orderly stacked with uniform interlayer spacing, they form a supercell along the *Z*-axis, leading to diffraction at specific (d*001*) values that reflect the total layer thickness, as it happens for α- or β-$Ni(OH)_2$. In this case, the XRD pattern reveals distinct "rational" reflections (*00l*) following the Bragg equation. In contrast, randomly interstratified structures produce non-periodical "irrational" reflections, influenced by component ordering and spacing variations. This effect, largely studied in the interstratification of clay minerals, allows to differentiate randomly interstratified materials from ordered stackings of layers or simple crystalline mixtures [54–57]. The XRD pattern of IS-$Ni(OH)_2$ exhibits similar interstratification patterns, corresponding to a brucite structure with *00l* reflections resulting from interference of interacting peaks of α- and β-$Ni(OH)_2$ phases with different layer spacing. IS-$Ni(OH)_2$ was early observed during the activation of Co-doped α-$Ni(OH)_2$, where partial removal of the interlayer anions induced the formation of a random stacking of interstratified α- and β-$Ni(OH)_2$ layers [27, 29, 30]. The formation of IS-$Ni(OH)_2$ was related to the amount of carbonates in the material in further studies on Mn-doped $Ni(OH)_2$, by assuming that α-β interstratification occurred when the amount of hydrated anions was not large enough for the complete swelling of brucite layers observed in α-$Ni(OH)_2$ [29, 30]. More recently, Dann and coworkers have suggested that IS-$Ni(OH)_2$ can be formed by interstratification of β-$Ni(OH)_2$ with nickel hydroxynitrates [25, 26]. This appears perfectly reasonable for basic salts formed by brucite-like layers with interlayer spacing near to the 7 Å value of α-$Ni(OH)_2$ [58–60].

Early preparations of IS-$Ni(OH)_2$ differed from usual preparations by avoiding the aging step after alkaline precipitation of α-$Ni(OH)_2$ at pH 10 [53, 61]. IS-$Ni(OH)_2$ was also obtained by alkali addition to a nickel nitrate solution by interrupting the precipitation when pH 12 was reached [21]. These conditions of synthesis have suggested IS-$Ni(OH)_2$ to be a metastable intermediate in the deanionization of α-$Ni(OH)_2$. The phase would be obtained by not allowing sufficient time for equilibration with the parent solution. The recent stabilization of IS-$Ni(OH)_2$ when the deanionization process is slowed down by lowering the aging temperature to 5 °C seems to support this interpretation [26].

Despite the higher specific capacitance and lower oxidation potential of the α- than the β-$Ni(OH)_2$ phase, the β phase is generally used in electrodes, due to its better stability in electrolyte solutions [62, 63]. Search

for possible exploitation of the potential of the α phase has led to attempts to stabilize this phase or to develop mixed α-β electrodes [7, 44, 64]. It has recently been suggested that the presence of carbonates improves the specific capacity of mixed α-β $Ni(OH)_2$ electrodes prepared by electrochemical deposition [65, 66]. The higher charge density of carbonates induces a lower solubility than the corresponding nitrates [67]. This suggests that carbonates can be strongly retained in the interlayer space of α-$Ni(OH)_2$, hindering the hydrothermal deanionization of α- to β-phase and favoring the stability of an IS-$Ni(OH)_2$ intermediate. This has prompted us to study the influence of carbonates on the formation and stability of the IS-$Ni(OH)_2$ phase by alkaline precipitation. Modifications in the precipitation solutions have allowed to modify the distribution of anions and to define a field of phase formation. The textural and electrochemical properties of the prepared IS-$Ni(OH)_2$ materials have been characterized and correlated to anion content and spectroscopic features.

Materials and methods

Samples were prepared by dropwise addition of 1 M nickel nitrate solution into basic solutions of NaOH or Na_2CO_3 at room temperature. Dropwise addition of NaOH solution allowed to keep constant pH 10 ± 0.1, near the conditions of minimal solubility of $Ni(OH)_2$ [68]. The precipitates were aged in their mother solution at 25 or 80 °C, filtered, washed with deionized water and dried at room temperature or 80 °C under air flow. The composition of the samples was indicated as $Ni(OH)_x(NO_3)_y(CO_3)_z{\cdot}wH_2O$, where y and z were evaluated by elemental analysis, w from the TG mass loss at 200 °C, and x was calculated from the molar ratios OH/Ni = 2–(NO_3/Ni + 2*CO_3/Ni), on the basis of the electroneutrality of the material. In the text, samples were named with a shorthand of their content of nitrate, carbonate and free water. For instance, sample N02-C14-W28 presents a composition $Ni(OH)_{1.70}(NO_3)_{0.02}(CO_3)_{0.14}{\cdot}0.28\ H_2O$. Synthesis conditions are reported in supplementary Table S1.

The amounts of carbonates and nitrates in the samples were measured using a Thermo-Fisher CHNS FLASH 2000 analyzer. A few milligrams of samples were brought at 1800 °C with a "FLASH" dynamic combustion. The elementary gases released by the decomposition were analyzed in a gas-chromatograph with a TCD detector. The mass loss of samples in thermal treatment was evaluated by thermal gravimetry (TG, DTG) on a Netzsch STA 409 PC LUXX® apparatus in air flow with a heating rate of 10 °C min^{-1}. Analytical data are reported in supplementary Table S2 and TG-DTG traces in Figures S1-S3. MS-coupled TG was carried out using a Seiko SSC/5200 thermal analyzer on about 20 mg of material. The powder was loaded into an open Pt crucible and heated under He stream at a heating rate of 10 °C min^{-1}. The thermal analyzer was equipped with a quadrupole mass spectrometer (ESS, GeneSys Quadstar 422) to analyze gases that evolved during heating. The measured masses, identified on the basis of the ratio m/z (mass-to-charge ratio), were m/z = 18 (H_2O), m/z = 30 (NO), m/z = 44 (CO_2). The gas analyses were performed in multiple ion detection mode (MID), allowing the qualitative determination of the evolved masses versus time or temperature. Possible contaminant cations were evaluated by energy-dispersive X-ray analysis (EDX) on a QUANTA 200F apparatus with Oxford Instruments X-Max N SDD detector: Sodium was detected in amounts smaller than atomic ratio Na/Ni 0.001.

X-ray powder diffraction (XRD) patterns were recorded on a Bruker AXS D8 Advance diffractometer with θ–θ Bragg–Brentano setting using Ni-filtered monochromatic CuKα radiation. Mering analysis of the XRD patterns of interstratified materials is detailed in the supplementary information. FTIR spectra were recorded using a Bruker Vector 22 equipped with a diamond ATR accessory (Bruker Platinum) and a DTGS detector. Textural properties were assessed by N_2 sorption at − 196 °C using a Tristar instrument (Micromeritics, Norcross, GA, USA) with improved secondary void. Samples were previously outgassed at 130 °C until stable 10 Pa pressure. The surface area was determined by the BET method, the pore volume by the αS method, and the pore size distribution by a DFT kernel [69]. Electrochemical tests were performed in a three-compartment, three-electrode batch cell using a potentiostat/galvanostat autolab (PGSTAT204, Metrohm, NOVA software). A saturated calomel electrode (SCE) and a Pt wire were used as a reference electrode and counter electrode, respectively. Cyclic voltammetry scans were recorded in NaOH 0.1 M between − 0.4 and 0.8 V versus *SCE* at a scan rate of 5 mV s^{-1}. Nearly 1 mg of sample powder was drop-casted from ethanol suspension on both sides of 1 cm^2 Ni plates.

Results and discussion

The XRD patterns of samples prepared by precipitation in NaOH solutions at different aging and drying temperatures are reported in Fig. 1. Sample N14-C15-W126 (Fig. 1a), aged and dried at room temperature, presents the expanded brucite pattern of α-Ni(OH)$_2$, with a 3.01 Å and c 8.19 Å [13, 70, 71]. A broad peak centered at 39°2θ (2.92 Å) is also observed, probably related to the superposition of turbostrating-tailed 101 and 102 reflections of α-Ni(OH)$_2$. [72]. N25-C14-W55 (Fig. 1b), the same sample dried at 80 °C instead of room temperature, presents a similar pattern except a peak shift reducing c to 7.37 Å, a value corresponding to the partially dehydrated phase that has been defined as α^{I}-Ni(OH)$_2$ by Rajamathi et al. [61]. The shrinkage of c corresponds to the narrowing of the interlayer space induced by the loss of water upon drying from the ratio H_2O/Ni 1.26 to 0.55.

Further dehydration to H_2O/Ni < 0.5, as observed in sample N19-C05-W21 (Fig. 1c), leads to the XRD pattern of an α/β-interstratified IS-Ni(OH)$_2$. Such a pattern is characterized by the presence of two peaks at 15.39 and 22.51°2θ angles. The corresponding d-spacing values (respectively, 5.79 and 3.95 Å) differ from the expected interlayer distances in β-Ni(OH)$_2$, with d*001* 4.60 Å, and α-Ni(OH)$_2$, with a pair of distances: d*001*, which ranges from approximately 7–10 Å, and d*002*, at half the d*001* value. The two characteristic IS-Ni(OH)$_2$ peaks correspond, respectively, to 001/001 and 002/001 mixed reflections, according to the nomenclature of interstratified clays, which lists first the parent phase with the smallest d, and separate them by a slash [56, 73]. The Mering analysis of the position of the peaks, in the hypothesis of random stacking of α and β layers, indicates the interstratification of 53% β-Ni(OH)$_2$ with an α-Ni(OH)$_2$ phase with c = 7.10 Å. The pattern of Fig. 1c also presents a weak peak at 19.36°2θ (4.58 Å), corresponding to a slow amount of poorly ordered β phase.

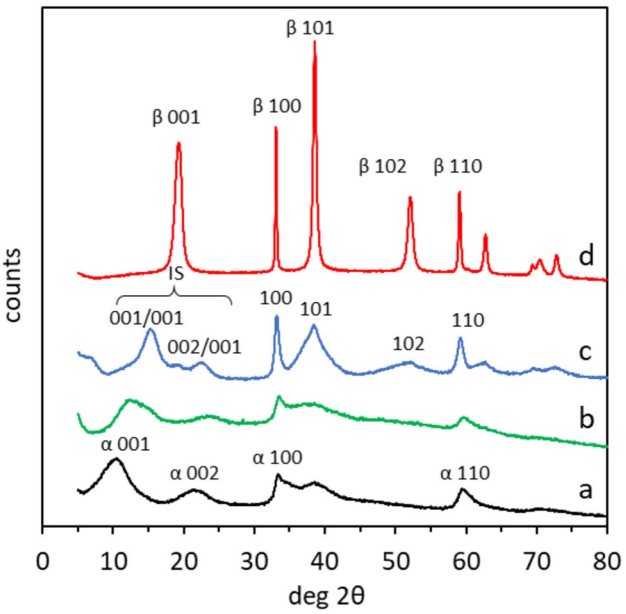

Figure 1 XRD patterns of samples precipitated in NaOH solution: α-Ni(OH)$_2$ N14-C15-W126 (*a*) and N25-C14-W55 (*b*), IS-Ni(OH)$_2$ N19-C05-W21 (*c*) and β-Ni(OH)$_2$ N02-C03-W06 (*d*).

Increasing the temperature of the aging treatment has been classically shown to favor the α-to-β transformation of Ni(OH)$_2$ [14, 20]. Samples aged in their parent solution at 80 °C were expected to feature the β-Ni(OH)$_2$ structure. Indeed, aging in the parent solution at 80 °C (sample N02-C03-W06, Fig. 1d) resulted in a nearly complete dehydration, the loss of almost all anions and the formation of a phase with β-Ni(OH)$_2$ diffraction pattern, a = 3.03 Å, c = 4.57 Å, and a light residual turbostratic broadening of reflections with $l \neq 0$ (Fig. 1d).

All samples prepared in NaOH solution presented both nitrate and carbonate anions. The nitrates are the counterions of the nickel precursor while the presence of carbonate results from the absorption of ambient CO_2 by the alkaline solution during the preparation.

The XRD patterns of samples prepared by precipitation in Na_2CO_3 solution at different aging and drying temperatures are reported in Fig. 2. The sample N00-C40-W129, aged and dried at room temperature (Fig. 2a), presents a diffraction pattern characteristic of layered material with similarities to the α-Ni(OH)$_2$ phase. A broad peak around 8.7°2θ would suggest a c parameter of 10.1 Å, attributed to a swollen material with two water molecules-thick interlayer [74]. A disordered occupation of the interlayer space could account for the lack of the expected 002 peak at 17.5°2θ. Remarkably, the 002 peak is well visible for α-Ni(OH)$_2$ samples with a lower amount of carbonates (see Fig. 1a and b). The position of the 100 and 110 peaks indicates an a parameter of 2.98 Å. Nitrates are present in trace amounts.

Drying at 80 °C brings to the extraction of nearly one-third of carbonate and water (sample N02-C21-W78, Fig. 2b). The 001 peak is shifted to 13.1°2θ, corresponding to c = 6.75 Å, a value showing partial

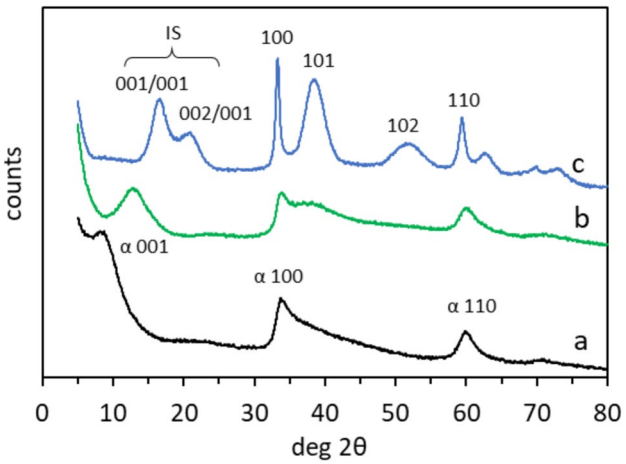

Figure 2 XRD patterns of samples precipitated in Na_2CO_3 solution: α-Ni(OH)$_2$ N00-C40-W129 (*a*) and N02-C21-W78 (*b*), IS-Ni(OH)$_2$ N02-C16-W37 (*c*).

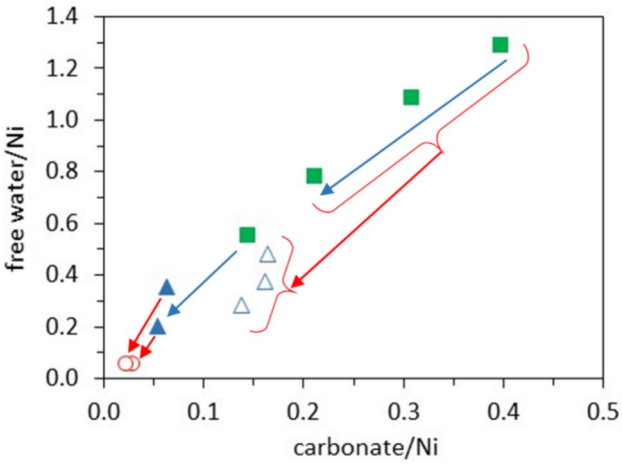

Figure 3 Phases observed as a function of carbonate and free water content: α-Ni(OH)$_2$ (green squares), IS-Ni(OH)$_2$ (blue triangles) and β-Ni(OH)$_2$ (red circles). Full symbols: samples aged at 25 °C; void symbols: samples aged at 80 °C. Blue arrows indicate the effects of drying at 80 °C. Red arrows connect samples aged at 25 and 80 °C.

dehydration of α-Ni(OH)$_2$. Aging the samples at 80 °C in their parent solution induces further dehydration to brucite-like layers but not their ordered stacking in the expected β phase. The 001/001 and 002/001 reflections at 16.85 and 21.05°2θ (respectively, 5.26 and 4.33 Å) of N02-C16-W37 (Fig. 2c) correspond to the splitting of the 001 peak of β-Ni(OH)$_2$ induced by interstratification with α-Ni(OH)$_2$ into IS-Ni(OH)$_2$. The Mering analysis of the XRD pattern, as detailed in the supplementary information, corresponds to a random interstratification of 72% β-Ni(OH)$_2$ with an α-Ni(OH)$_2$ phase with $c = 6.85$ Å. The hk0 reflections of the diffraction pattern allow to measure an *a* parameter of the brucite layers of 3.02 Å.

The effect of the use of Na_2CO_3 in the synthesis can be rationalized by considering the phases obtained at 25 and 80 °C as a function of their content of carbonate and interlayer water, as represented in Fig. 3. Samples aged at 25 °C (full symbols) present α- or IS-Ni(OH)$_2$ phases according to their content of carbonate: α-Ni(OH)$_2$ is present at ratio CO_3^{2-}/Ni higher than 0.15. and IS-Ni(OH)$_2$ for a ratio lower than 0.06. Drying at 80 °C (blue arrows) induces simultaneous losses of water and anions and, for the less carbonate-rich samples, an α- to IS transformation.

Aging treatment in the parent solution at 80 °C, highlighted by red arrows in Fig. 3, induces the formation of different phases (void symbols) according to the carbonate content of the material. Systems with CO_3^{2-}/Ni ≤ 0.15 are nearly completely dehydrated and form β-Ni(OH)$_2$ independently from the phase, α- or IS-Ni(OH)$_2$, formed at 25 °C. Systems with CO_3^{2-}/Ni > 0.20, that form α-Ni(OH)$_2$ at 25 °C, form IS-Ni(OH)$_2$ at 80 °C. The high carbonate content is at the origin of the stability of the interstratified material at 80 °C. It can be recalled that the retention of anions was proposed as the mechanism for the formation of IS-Ni(OH)$_2$. Delmas and coworkers suggested that a partial deanionization of α-Ni(OH)$_2$ was at the origin of local variations of the interlayer space, leading to the random stacking of differently swollen brucite layers [27–30].

The IS-Ni(OH)$_2$ samples present different values of the split of the 001/001 and 002/001 peaks formed by interstratification of the 001 reflection of β-Ni(OH)$_2$ with the 001 and 002 reflections of α^1-Ni(OH)$_2$. The peak split changes between samples prepared in Na_2CO_3 or NaOH solutions. The split value was 1.03 ± 0.09 and 1.78 ± 0.08 Å for, respectively, carbonate-rich and carbonate-poor IS-Ni(OH)$_2$. The presence of a β-Ni(OH)$_2$ impurity in the carbonate-poor samples (Fig. 1c) likely increases the α/β ratio in the interstratification and accounts for the wider split of peaks [55, 56].

The evolution of the interaction of the anions with their environment in the dehydration-deanionization process can be investigated by FTIR spectroscopy. Figure 4 shows the FTIR spectra of N02-C03-W06,

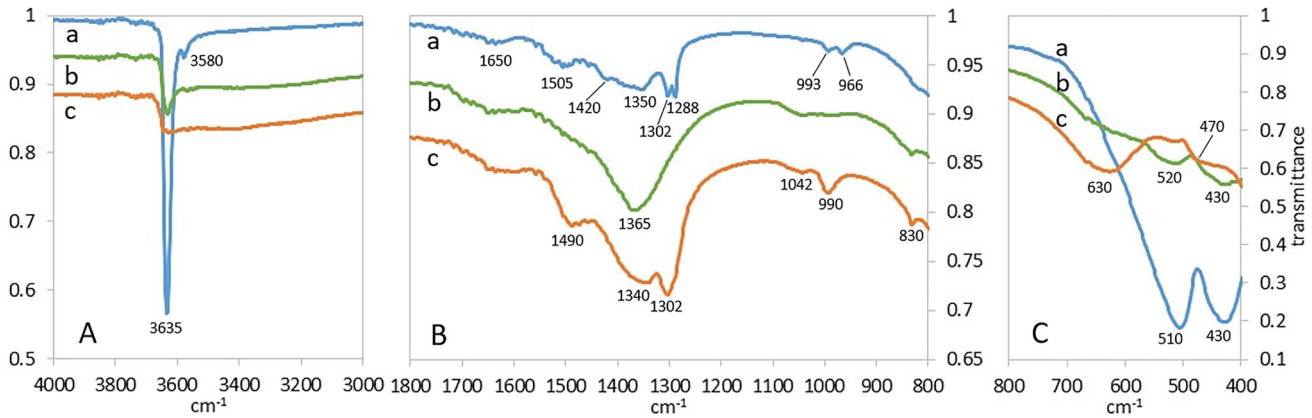

Figure 4 FTIR spectra of β-Ni(OH)$_2$ N02-C03-W06 (*a*), IS-Ni(OH)$_2$ N02-C16-W37 (*b*), α-Ni(OH)$_2$ N25-C14-W55 (*c*) in the O–H stretching (**A**), anion bending (**B**) and structural vibration (**C**) regions. Traces are shifted for sake of clarity.

a β-Ni(OH)$_2$ sample retaining traces of anions and water (curve a), N02-C16-W37, a carbonate-rich IS-Ni(OH)$_2$ sample (curve b), and N25-C14-W55, an *α*-Ni(OH)$_2$ sample prepared in NaOH solution, containing both nitrate and carbonate anions (curve c).

In the O–H stretching region, the curve a of Fig. 4A presents the typical peaks of β-Ni(OH)$_2$ at 3635 and 3580 cm^{-1} [71], whereas the *α*-Ni(OH)$_2$ spectrum (curve c) presents a broad signal of hydrogen-bonded OH in the region 2600–3640 cm^{-1}, corresponding to the interaction of hydroxyls with anions and interlayer water [75]. The spectrum of IS-Ni(OH)$_2$ (curve b) presents the same broad signal accompanied by a peak at 3630 cm^{-1}, indicating the simultaneous presence of bonded and free structural hydroxyls.

In all spectra, vibrations of anions in several configurations are visible in the region of bending vibrations (Fig. 4B). Isolated CO_3^{2-} and NO_3^- anions present trigonal molecular symmetry D_{3h} that is lowered to C_{2v} point group by any asymmetric interaction of the anion with the surroundings [76, 77]. In D_{3h} symmetry, the ν_1 vibration mode (symmetric C–O or N–O stretching) is IR-inactive and is activated in C_{2v} symmetry in the region 950–1050 cm^{-1}. The lowering of molecular symmetry also induces a splitting of the ν_3 antisymmetric stretching vibration near 1300 cm^{-1}. An O–H bending band of water at 1650 cm^{-1} is visible in all spectra.

The spectrum of *α*-Ni(OH)$_2$ N25-C14-W55 (curve c), containing more nitrate than carbonate, presents a ν_1 band at 990 cm^{-1} and splitted ν_3 bands at 1302 and 1490 cm^{-1}, corresponding to C_{2v} nitrates in strong interaction with the layers [4, 32]. A broad complex band between 1340 and 1420 cm^{-1} includes carbonate and D_{3h} nitrate components. The presence of a ν_1 band at 1042 cm^{-1} indicates that also carbonates are in C_{2v} symmetry.

The spectrum of the carbonate-rich IS-Ni(OH)$_2$ N02-C16-W37 (curve b) presents a broad ν_3 carbonate band at 1365 cm^{-1} with a shoulder at 1420 cm^{-1}, in a typical hydrotalcite-like configuration [78]. The limited splitting of the ν_3 band to C_{2v} symmetry has been generally attributed to interaction with layer hydroxyls or interlayer water [79, 80]. Wegrzyn et al. have observed by in situ DRIFT that the ν_3 splitting increases with partial dehydration of the hydrotalcite, suggesting that the interlayer water favor a symmetric environment for the carbonate anion and possibly masks more direct interactions with the layer [81]. In our sample, the presence of a weak band at 1042 cm^{-1} confirms the IR activation of the ν_1 band and the shift of carbonate away from the D_{3h} symmetry [76]. The ν_2 bending band at 830 cm^{-1} is due to the presence of minor nitrates.

The spectrum of the β-Ni(OH)$_2$ sample N02-C03-W06 (curve a) presents the bands of residual anions, mainly at low C_{2v} symmetry, suggesting that only the most tightly bound anions have been left after dehydration. Peak pairs at 966–993 and 1288–1302 cm^{-1} correspond to split symmetric and antisymmetric stretching. A broad band at 1505 cm^{-1} corresponds to a splitted ν_3 stretch. The wider ν_3 splitting in β- than in *α*-Ni(OH)$_2$ is suggestive of multiple interactions of the nitrate anions [76]. In a similar way, the axis of nitrate anions in the hydrotalcites is at a wider angle with the brucite-like

layer axis, also due to crowding of the monovalent anions in the interlayer, and the direct interaction with the layers justifies a large split of the ν_3 band [82]. Retained anions account for a limited residual turbostratic disorder in the β-Ni(OH)$_2$ sample. The superposition of nitrate and carbonate bands is also significant in the region 1350–1420 cm^{-1}, and the presence of D_{3h} nitrates cannot be excluded.

Broad bands in curve c of Fig. 4C at 470 and 630 cm^{-1} are in good agreement with the lattice modes of α-Ni(OH)$_2$ [14], whereas the intense bands at 430 and 510 cm^{-1} of curve a correspond to the structural vibrations of the brucite-like β-Ni(OH)$_2$ [83]. In the same region, the IS-Ni(OH)$_2$ spectrum of curve b presents broad bands at 430, 520, and 650 cm^{-1}, suggesting the presence of both α- and β-Ni(OH)$_2$ features.

The FTIR data support the hypothesis of several configurations of the anions in the samples. A large fraction of nitrates is stretched in an asymmetric configuration, as required by the compensation of the positive charge of the layers [82]. The wide splitting of the ν_3 mode (190–215 cm^{-1}) is compatible with a direct bonding of the anion with the Ni^{2+} cations [76]. In this case, the substitution of a hydroxy group by the anion would ensure the electroneutrality of the material. It would be tempting to attribute the cation–anion bonding to incomplete hydrolysis of nickel-bearing synthesis precursors, as suggested by the modelization of equilibria between species in the synthesis solution [20]. The carbonate anions present instead a hydrotalcite-like type of symmetry, with a limited ν_3 splitting of about 50 cm^{-1} [78]. The similitude with hydrotalcite is suggestive of multiple interactions of the divalent anion with both layer and interlayer water [79, 80].

Thermal decomposition of nickel hydroxides can provide some information on the reactivity of different anions. Thermal gravimetry (TG) with mass analysis of the emitted gases (TG-MS) allows us to monitor the temperature of release of different degradation products. Figure 5 shows the TG and DTG (differential thermal gravimetry) curves of two IS-Ni(OH)$_2$ and two α-Ni(OH)$_2$ samples with different carbonate and nitrate contents. The samples had been previously dried at 80 °C and re-exposed at ambient air. The patterns of mass loss correspond to what is usually observed for other hydroxides, like hydrotalcite LDH, with a first mass loss around 100 °C, attributed to the desorption of interlayer water, and a main peak between 250 and 300 °C, corresponding to dehydroxylation and deanionization [84–86]. Complete TG and DTG data are provided in the supplementary material (Table S2 and Figures S1-S3). The mass loss in the first dehydration peak was in the range of 12–21% for α-Ni(OH)$_2$, 3–8% for IS-Ni(OH)$_2$ and up to 1% for β-Ni(OH)$_2$ samples. Further mass loss at temperature values higher than 200 °C was in the same 21–25% range for α-Ni(OH)$_2$ and IS-Ni(OH)$_2$ samples and was 20% for the β-Ni(OH)$_2$ samples, near to the value 19.4% expected for the dehydroxylation of Ni(OH)$_2$ to NiO. It can be observed that, in the case of nitrate-richest samples (curves b and c), the mass loss beyond 200 °C includes the main DTG peak around 250–300 °C and a minor peak between 350 and 450 °C.

Mass spectroscopy (MS) of the evolved decomposition products allows to identify the molecules that evolved in each decomposition step. In this way, the TG and DTG curves of Fig. 5 can be interpreted through the mass spectra of evolved gases as shown in

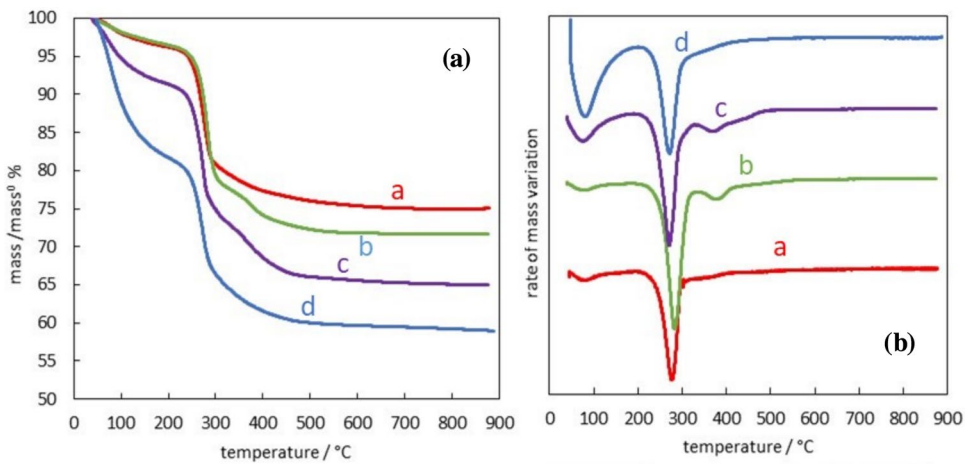

Figure 5 TG (**a**) and DTG (**b**) traces of samples IS-Ni(OH)$_2$ N02-C14-W28 (*a*) and N19-C05-W21 (*b*), and α-Ni/OH)$_2$ N25-C14-W55 (*c*) and N00-C40-W129 (*d*).

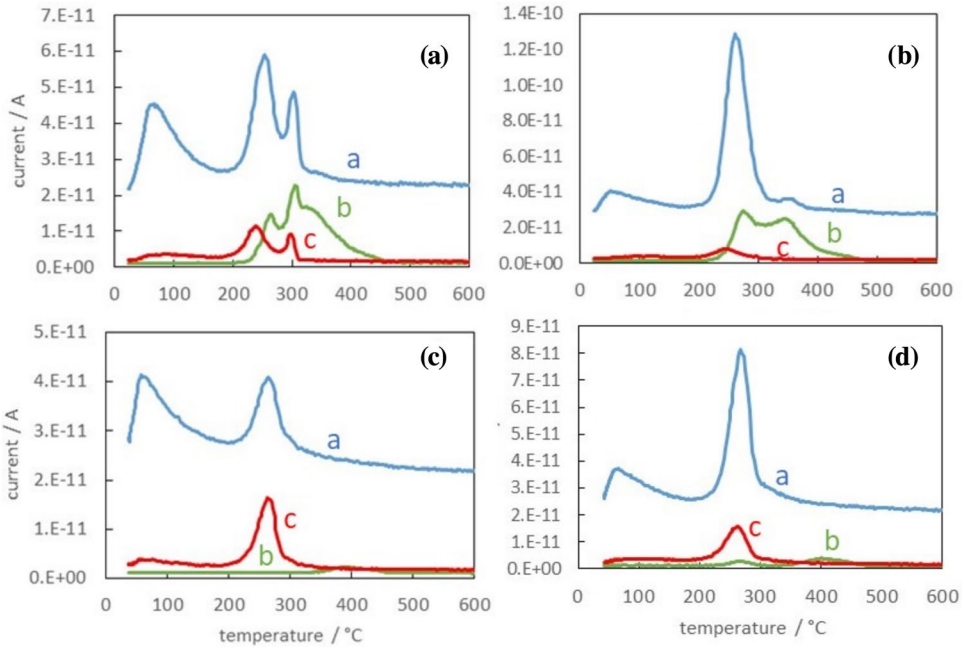

Figure 6 TG-MS curves of Ni-rich α-Ni/OH)$_2$ N25-C14-W55 (**A**) and IS-Ni(OH)$_2$ N19-C05-W21 (**B**), and Ni-poor α-Ni/OH)$_2$ N02-C21-W78 (**C**) and IS-Ni(OH)$_2$ N06-C16-W48 (**D**). Curves of monitored masses 18 (*a*), 30 (*b*), and 44 (*c*). The intensity of mass 18 and 30 are traced as multiplied by 4 for sake of visibility.

Fig. 6. Monitored masses were mass 18, corresponding to water development by dehydration or condensative dehydroxylation, mass 44, corresponding to CO_2 released by carbonate decomposition, and mass 30, corresponding to NO^+, issued by the decomposition of NO_2 released by the nitrate decomposition [87]. Mass 46, corresponding to NO_2, was also monitored but only traces were observed in parallel with the NO^+ evolution, as expected by the pattern of ionization in MS conditions [85].

The first peak of mass loss corresponds to the desorption of interlayer water, as expected. However, a limited amount of CO_2 is released below 200 °C. Early development of CO_2 has been often observed in Ni-LDH and is sometimes attributed to desorption from the external surface without further characterization of the adsorption site [75, 79, 86]. It could be interesting to correlate this small emission of CO_2 to the mechanism postulated by Kanezaki for the decarbonatation of LDH, similar to the desorption of CO_2 from carbonated aqueous solution, with the formation of two hydroxyls per emitted CO_2 [88, 89]. This reaction pathway, initially suggested to be active beyond 200 °C, has been calculated to be possible also at a lower temperature, albeit less thermodynamically favored than direct emission of the hydration water [90].

The main peak around 270 °C corresponds to the release of water from dehydroxylation and the emission of the decomposition products of anions. In all samples, the release of CO_2 is always connected with the development of water, in strict parallel with what is systematically observed in the case of hydrotalcites [85, 86]. No products of the decomposition of carbonates are observed after the condensation of the hydroxides, with the corresponding formation of NiO, also due to the instability of nickel carbonate above 300 °C [91].

The measurement of NO^+, from the decomposition of nitrates, does not follow the same pattern, being always shifted to a higher temperature than the development of CO_2^+. The retention of nitrates at a higher temperature than carbonates has already been observed in the thermal decomposition of α-Ni(OH)$_2$ [92, 93], nickel hydroxynitrates [94] and Ni-bearing hydrotalcites [81, 86, 95]. Indeed, a significant fraction of NO^+—often nearly half- is released at higher temperature than the release of water, hence after the dehydroxylation has been completed [96]. It has to be assumed that such NO^+ release corresponds to the degradation of nitrates retained in the nickel oxides formed by Ni(OH)$_2$ dehydroxylation.

The presence of Ni^{3+} sites could represent a valid explanation for a higher temperature of retention of anions. The behavior of samples with similar amount of nitrates and carbonates, like α-Ni/OH)$_2$ N25-C14-W55 (Fig. 6A) is especially interesting. In the presence of high amount of nitrates also a fraction of carbonates is retained at a higher temperature,

being released at 300 °C, after the main peak of CO_2 desorption at 230 °C. It appears that Ni^{3+} species, induced by the decomposition products of nitrates, are able to more strongly retain all kinds of anions. The formation of Ni^{3+} sites in NiO by the action of NO_x has been early assessed by surface FTIR studies [97]. Chmielarz et al. connected the retention of nitrate anions to possible strong adsorption on Ni^{3+} sites formed by oxidation of Ni^{2+} by the NO_x/O_2 atmosphere formed in the initial nitrate decomposition [95]. Brockner et al. monitored the thermal decomposition of $Ni(NO_3)_2{\cdot}6H_2O$ by quasi-isothermal thermal gravimetry in an inert atmosphere [98]. They interpreted the final steps of mass loss as the formation of "Ni_2O_3" at 250 °C, followed by the reduction of "Ni_2O_3" to NiO at 400 °C after evacuation of the oxidizing atmosphere. Due to this instability, the Ni^{3+}-bearing phase could not be detected by ex situ XRD. Fingerle et al. studied the behavior of "$Ni_2O_{3,}$" which they defined as an ill-defined oxygen-rich NiO_x phase, by XPS of thin layers of photo-oxidized NiO [99]. They confirmed the thermal instability of Ni_2O_3 formed at room temperature, the amount of "Ni_2O_3" being halved at 200 °C and ten times reduced at 400 °C. They also observed a hydration-dehydration equilibrium of Ni_2O_3 with $Ni(OH)_2$ and NiOOH. It appears that the transient formation of Ni^{3+} intermediates by-products of nitrate decomposition can be a plausible explanation for the high-temperature retention of anions and represent a general trend in the thermal decomposition of nitrate-bearing Ni materials.

The nature of IS-$Ni(OH)_2$ upon thermal treatment can be studied by XRD of samples calcined at different temperatures under air flow, as reported in Fig. 7 for sample N02-C14-W28. The material retained the IS-$Ni(OH)_2$ pattern when calcined at 210 °C in air flow. The interstratification splitting of the 100 peak of β-$Ni(OH)_2$ decreases from 1.06 to 0.79 Å, and a Mering analysis suggests a decrease of the contribution of the water- and anion-rich α-$Ni(OH)_2$ component from 33 to 23%. When calcined at 210 °C, the IS-$Ni(OH)_2$ pattern presents also a weak 200 peak of NiO at 43.4°2θ. After calcination at 230 °C, NiO is the only phase present, with very broad peaks. The peaks of NiO become narrower with calcination at higher temperatures and a Scherrer estimate of the crystallite size gives 3.4, 10.2 and 20.6 nm for samples calcined at, respectively, 230, 400, and 600 °C. NiO was always the only oxide phase observed, suggesting that more oxidized materials

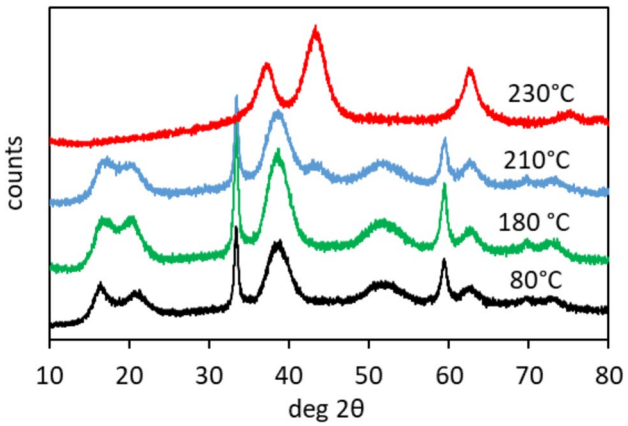

Figure 7 XRD pattern of IS-$Ni(OH)_2$ sample N02-C14-W28 calcined at different temperatures.

could be unstable in the calcination conditions –or not XRD detectable- throughout the field of temperature.

Mesoporosity could represent an important asset in the control of the accessibility of electrolytes to the surface of electrode materials or in their application as superconductors [100–103]. Textural information on our materials was collected by nitrogen sorption at 77 K, measured on samples outgassed at 130 °C. Isotherms and pore size distribution from the desorption branch of the isotherms are reported in Fig. 8. Surface area and pore volume data are reported in Table 1.

α-$Ni(OH)_2$ samples (Fig. 8A) feature type II isotherms, typical of macroporous adsorbents according to the IUPAC classification [104]. This suggests that the loss of interlayer water led to close packing of the brucite-like layers and only the outer surface of the nanocrystals was accessible. It is worth observing that much larger surface areas can be obtained by drying methods that prevent meniscus collapse and aggregation of the nanocrystals [5, 105, 106].

Both IS- and β-$Ni(OH)_2$ samples feature a type IV(a) mesoporous isotherm but the shapes of their hysteresis loops differ. IS-$Ni(OH)_2$ samples (Fig. 8B) present an H2 hysteresis loop, typical of bottle-neck mesopores with narrow pore mouths. Sample N06C16W48 features an H2(b) hysteresis, corresponding to a distribution of pore mouth size from 5 to 10 nm. Electrodeposited mixtures of α- and β-$Ni(OH)_2$ were shown to present isotherms of the same type, attributed to the porosity of assembled nanosheets [3]. Sample N02C16W37 (curve d in Fig. 5B), with smaller pores, presents a sudden cavitation at p/p^0 0.47, typical of H2(a) hysteresis and cavities with pore mouth smaller

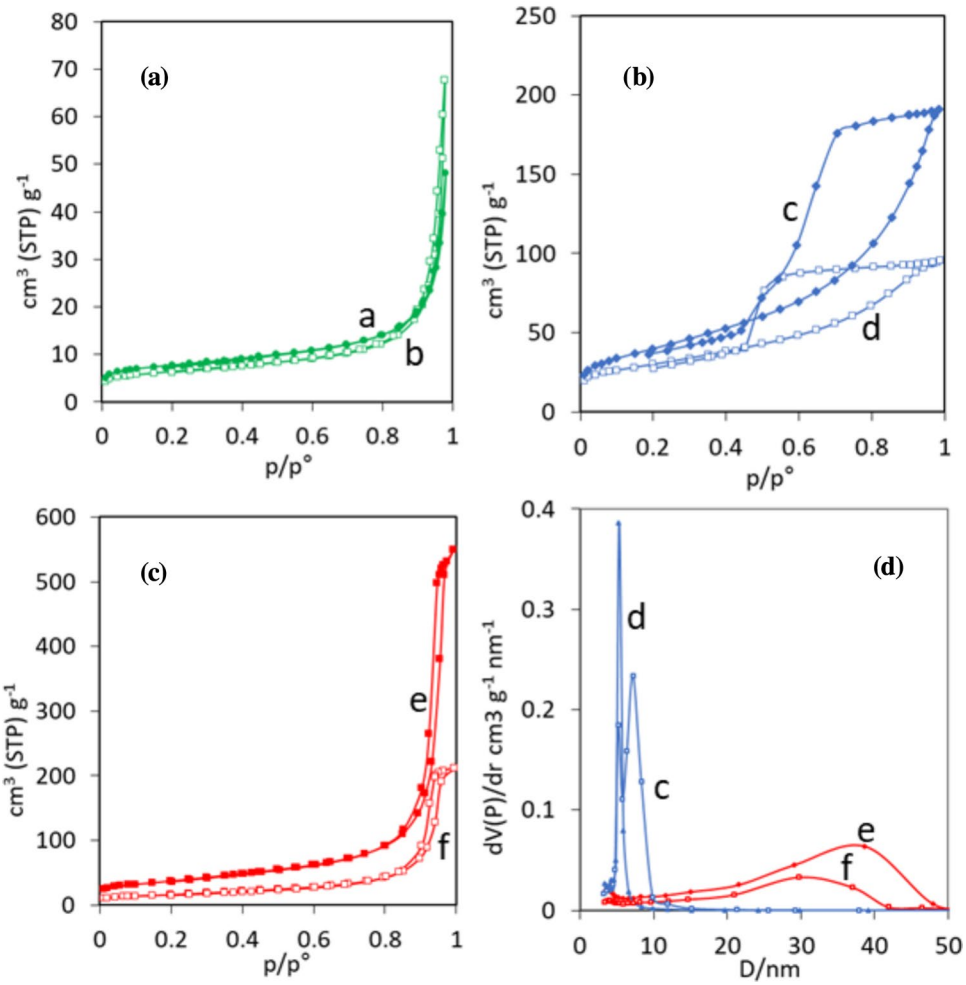

Figure 8 N_2 sorption isotherms of **A** α-, **B** IS- and **C** β-$Ni(OH)_2$ samples and **D** pore size distributions. Individual samples are identified by small letters in Table 1 of the text.

Table 1 Textural data of α-, IS- and β-$Ni(OH)_2$ from N_2 sorption

Letter in Fig. 5	Sample	Phase	Surface area	Pore volume	Average pore size
		$Ni(OH)_2$	$m^2\ g^{-1}$	$cm^3\ g^{-1}$	nm
a	N01C31W109	α	28	0.06	n. a
b	N14C15W126	α	23	0.08	n. a
c	N06C16W48	IS	144	0.28	12
d	N02C16W37	IS	107	0.14	8
e	N02C03W06	β	134	0.71	37
f	N01C02W06	β	8	0.31	29

than 5 nm [107]. β-$Ni(OH)_2$ samples (Fig. 8C) present larger pores with a type IV(a) isotherm and H1 hysteresis, typical of an open mesopore network, related to intergranular porosity. Literature β-$Ni(OH)_2$ samples present lower surface area and apparently similar isotherms [100]. However, they differ from our results by the absence of an inflection point at high relative pressure and should possibly be considered as type II isotherms [104].

Applications of IS-$Ni(OH)_2$ as electrode material require an evaluation of its electrochemical potential. Cyclic voltammetry curves of carbonate-bearing N02-C14-W28 are shown in Fig. 9. The anodic oxidation of Ni^{2+} to Ni^{3+} starts at 0.37 V and presents two maxima

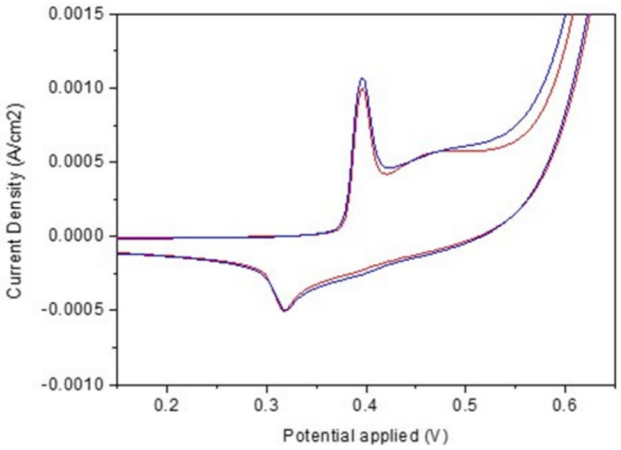

Figure 9 Cyclic voltammetry curves of drop-casted IS-Ni(OH)$_2$ N02-C14-W28 in NaOH 0.1 M with scanning rate 5 mV s.$^{-1}$. Scans 2 (red) and 3 (blue).

at 0.40 and 0.47 V before the oxygen evolution reaction (OER). The cathodic reduction of the γ-NiOOH formed presents a maximum at 0.32 V and is completed only at negative potential. This pattern was well reproducible in successive cycles.

It seems appropriate to correlate the two anodic peaks in the charge run to the oxidation of α-Ni(OH)$_2$ and β-Ni(OH)$_2$, usually observed, respectively, near 0.35 V and 0.45 V [102, 108–110]. The presence of two signals in the oxidation of α-Ni(OH)$_2$ has been often observed. The second peak has been sometimes attributed to the oxidation of β-Ni(OH)$_2$ formed by in situ dehydration of α-Ni(OH)$_2$ [111, 112]. In these cases, the two-peak pattern evolved to one-peak in successive cycles, as the α-component was not restored in the cathodic reoxidation step. This is not observed in the case of IS-Ni(OH)$_2$, when the repeatability of the two-signal pattern of Fig. 9 suggests that the presence of the two components can be a stable feature of IS-Ni(OH)$_2$. It is also interesting to consider the possible role of the anions in the electrochemical behavior, taking into account the onset of oxidation at 0.3 eV on $Ni_2CO_3(OH)_2$ supercapacitor material, featuring carbonate-bridged puckered layers of nickel hydroxide [113], as well as the dependence of the capacitance of α-Ni(OH)$_2$ on the nature of the interlayer anion [114].

Conclusions

Monitoring the precipitation of Ni(OH)$_2$ phases from alkaline conditions has confirmed that interstratified IS-Ni(OH)$_2$ is an intermediate in the dehydration-deanionization process of α- to β-Ni(OH)$_2$. The critical step in the α-to-β transformation is the aging of the precipitate in the parent solution. During the initial precipitation of nickel hydroxide, high supersaturation induces the retention of anions in a metastable α-Ni(OH)$_2$ phase. Temperature and alkalinity of the aging process control the shift from hydrated anion-rich metastable materials toward more ordered dehydrated β-Ni(OH)$_2$. Throughout the process, the non-uniform removal of anions is at the origin of the interstratification of brucite-like layers with different interlayer spacing, giving rise to the IS-Ni(OH)$_2$ phase. IS-Ni(OH)$_2$ can be formed in the presence of either nitrate or carbonate anions but the nature of the anion affects the evolution of the parent material. Carbonate anions, more tightly bound to the brucite layers, stabilize IS-Ni(OH)$_2$ materials when aged at a temperature as high as 80 °C, conditions in which nitrate-rich materials are fully dehydrated and deanionised to β-Ni(OH)$_2$. FTIR spectroscopy indicates that IS-Ni(OH)$_2$ shares structural elements of both interstratified α and β layers. They present surface areas higher than 100 m^2 g^{-1} and peculiar adsorption patterns, indicating that the interstratification induces the formation of ink-bottle mesopores.

IS-Ni(OH)$_2$ materials are thermally stable up to nearly 200 °C, the temperature at which they are deanionized and dehydroxylated to nanocrystalline NiO. The TG-MS monitoring of the thermal activation evidences the formation of intermediate Ni^{3+} species by the reaction with NO_x emitted by the degradation of nitrates. The general phenomenon is a witness of the effectiveness of Ni^{2+}-hydroxides as redox materials. The cyclic voltammetry pattern of IS-Ni(OH)$_2$ shows features of both α- and β-Ni(OH)$_2$, with an initial reduction potential of 0.37 V. Given the good thermal stability and the high accessibility to incoming ions and molecules, carbonate-stabilized mesoporous IS-Ni(OH)$_2$ emerge as promising materials for electrocatalytic applications.

Declarations

Conflict of interest The authors declare that they have no conflict of interest.

Supplementary Information The online version contains supplementary material available at https://doi.org/10.1007/s10853-025-10735-7.

References

[1] McBreen J (2021) Nickel Hydroxides. In: Daniels C, Besenhard JO (eds) Handbook of battery materials. Wiley-VCH, Weinheim, pp 149–168. https://doi.org/10.1002/9783527637188.ch5

[2] Palacin MR (2009) Recent advances in rechargeable battery materials: a chemist's perspective. Chem Soc Rev 38:2565–2575. https://doi.org/10.1039/b820555h

[3] Wang M, Feng QP, Wu XH, Huang GW (2017) Synthesis of high specific surface area Co−Ni$(OH)_2$ by a self-template secondary growth method and its application as a cathode material in the nickel metal hydride battery. Cryst Growth Des 17:1258–1263. https://doi.org/10.1021/acs.cgd.6b01652

[4] Ash B, Nalajala VS, Popuri AK, Subbaiah T, Minakshi M (2020) Perspectives on nickel hydroxide electrodes suitable for rechargeable batteries: electrolytic versus chemical synthesis route. Nanomaterials 10:1878. https://doi.org/10.3390/nano10091878

[5] Zhu Y, Cao C (2015) Remarkable electrochemical lithium storage behaviour of two-dimensional ultrathin a-Ni$(OH)_2$ nanosheets. RSC Adv 5:83757–83763. https://doi.org/10.1039/c5ra15514b

[6] Yao J, Li Y, Pan G, Jin X, Luo K, Le S (2021) Electrochemical property of hierarchical flower-like α-Ni$(OH)_2$ as an anode material for lithium-ion batteries. Solid State Ion 363:115595. https://doi.org/10.1016/j.ssi.2021.115595

[7] Gao M, Sheng W, Zhuang Z, Fang Q, Gu S, Jiang J, Yan Y (2014) Efficient water oxidation using nanostructured α-nickel-hydroxide as an electrocatalyst. J Am Chem Soc 136:7077–7084. https://doi.org/10.1021/ja502128j

[8] Goldsmith ZK, Harshan AK, Gerken JB, Vörös M, Galli G, Stahl SS, Hammes-Schiffer S (2017) Characterization of NiFe oxyhydroxide electrocatalysts by integrated electronic structure calculations and spectroelectrochemistry. Proc Natl Acad Sci USA 114:3050–3055. https://doi.org/10.1073/pnas.1702081114

[9] Agoston R, Sayeed MA, Jones MWM, de Jonge MD, O'Mullane AP (2019) Monitoring compositional changes in Ni$(OH)_2$ electrocatalysts employed in the oxygen evolution reaction. Analyst 144:7318–7325. https://doi.org/10.1039/c9an01905g

[10] Rossini PO, Laza A, Azeredo NFB, Gonçalves JM, Felix FS, Araki K, Angnes L (2020) Ni-based double hydroxides as electrocatalysts in chemical sensors: A review. Trends Anal Chem 126:115859. https://doi.org/10.1016/j.trac.2020.115859

[11] Zhang R, Ran T, Cao Y, Zhang Q, Dong F, Yang G, Zhou Y (2020) Surface Hydrogen atoms promote oxygen activation for solar light-driven NO oxidization over monolithic α-Ni$(OH)_2$/Ni foam. Environ Sci Technol 54:16221–16230. https://doi.org/10.1021/acs.est.0c05635

[12] Natta G (1925) Struttura cristallina degli idrati di cadmio e di nichel. Rend Accad Lincei 6:495–501

[13] Bode H, Dehmelt K, Witte J (1996) Zur kenntnis der nickelhydroxidelektrode-I. Über das nickel (II)-hydroxidhydrat. Electrochim Acta 11:1079–1087. https://doi.org/10.1016/0013-4686(66)80045-2

[14] Hall DS, Lockwood DJ, Bock C, MacDougall BR (2015) Nickel hydroxides and related materials: a review of their structures, synthesis and properties. Proc R Soc A 471:20140792. https://doi.org/10.1098/rspa.2014.0792

[15] Faure C, Delmas C, Fouassier M (1991) Characterization of a turbostratic α-nickel hydroxide quantitatively obtained from an $NiSO_4$ solution. J Power Sources 35:279–290. https://doi.org/10.1016/0378-7753(91)80112-B

[16] Delahaye-Vidal A, Beaudoin B, Sac-Epée N, Tekaia-Elhsissen K, Audemer A, Figlarz M (1996) Structural and textural investigations of the nickel hydroxide electrode. Solid State Ion 84:239–248. https://doi.org/10.1016/0167-2738(96)00030-6)

[17] Vishnu Kamath P, Therese GHA, Gopalakrishnan J (1997) On the existence of hydrotalcite-like phases in the absence of trivalent cations. J Solid State Chem 128:38–41. https://doi.org/10.1006/jssc.1996.7144

[18] Taibi M, Jouini N, Rabu P, Ammard S, Fiévet F (2014) Lamellar nickel hydroxy-halides: anionic exchange, synthesis, structural characterization and magnetic behavior. J Mater Chem C 2:4449–4460. https://doi.org/10.1039/c3tc32530j

[19] Sanchis-Gual R, Jaramillo-Hernández C, Hunt D, Seijas-Da SÁ, Mizrahi M, Marini C, Abellán G (2024) Influence of crystallographic structure and metal vacancies on the oxygen evolution reaction performance of Ni-based layered hydroxides. Chem Eur J 30:e202303146. https://doi.org/10.1002/chem.202303146

[20] Soler-Illia GJAA, Jobbagy M, Regazzoni AE, Blesa MA (1999) Synthesis of nickel hydroxide by homogeneous alkalinization precipitation mechanism. Chem Mater 11:3140–3146. https://doi.org/10.1021/cm9902220

[21] Ramesh TN, Vishnu Kamath P (2006) Synthesis of nickel hydroxide: effect of precipitation conditions on phase selectivity and structural disorder. J Power Sour 156:655–661. https://doi.org/10.1016/j.jpowsour.2005.05.050

[22] Le Bihan S, Figlarz M (1972) Croissance de l'hydroxyde de nickel Ni$(OH)_2$ à partir d'un hydroxyde de nickel turbostratique. J Cryst Growth 13(14):458–461. https://doi.org/10.1016/0022-0248(72)90280-1

[23] Hall DS, Lockwood DJ, Poirier S, Bock C, MacDougall BR (2014) Applications of in Situ Raman spectroscopy for identifying nickel hydroxide materials and surface layers during chemical aging. ACS Appl Mater Interfaces 6:3141–3149. https://doi.org/10.1021/am405419k

[24] Chen Z, Fan Q, Huang M, Cölfen H (2023) The structure, preparation, characterization, and intercalation mechanism of layered

hydroxides intercalated with guest anions. Small 19:2300509. https://doi.org/10.1002/smll.202300509
[25] Wallbridge SP, Lawson K, Catling AE, Kirk CA, Dann SE (2022) Synthesis and spectroscopic identification of nickel and cobalt layered hydroxides and hydroxynitrates. Dalton Trans 51:18010–18023. https://doi.org/10.1039/d2dt03166c
[26] Lawson K, Wallbridge SP, Catling AE, Kirk CA, Dann SE (2023) Determination of layered nickel hydroxide phases in materials disordered by stacking faults and interstratification. J Mater Chem A 11:789–799. https://doi.org/10.1039/d2ta07655a
[27] Delmas C, Faure C, Borthomieu Y (1992) The effect of cobalt on the chemical and electrochemical behaviour of the nickel hydroxide electrode. Mater Sci Eng B 13:89–96. https://doi.org/10.1016/0921-5107(92)90147-2
[28] Demourgues-Guerlou L, Braconnier JJ, Delmas C (1993) Iron-substituted nickel oxyhydroxides ans hydroxides obtained by chimie douce. J Solid State Chem 104:359–367. https://doi.org/10.1006/jssc.1993.1171
[29] Guerlou-Demourgues L, Denage C, Delmas (1994) New manganese-substituted nickel hydroxides Part 1. Crystal chemistry and physical characterization. J Power Sources 52:269–274. https://doi.org/10.1016/0378-7753(94)02023-X
[30] Guerlou-Demourgues L, Delmas C (1994) New manganese-substituted nickel hydroxides Part 2. Interstratification process upon ageing. J Power Sources 52:275–281. https://doi.org/10.1016/0378-7753(94)02024-8
[31] Louër M, Louër D, Grandjean D (1973) Etude structurale des hydroxynitrates de nickel et de zinc I classification structurale. Acta Cryst B 29:1696–1703. https://doi.org/10.1107/S0567740873005285
[32] Jahangiri S, Mosey NJ (2018) Molecular structure and interactions of water intercalated in nickel hydroxide. Phys Chem Chem Phys 20:11444. https://doi.org/10.1039/c8cp00070k
[33] Oswald HR (1961) Über natürlichen und künstlichen Gerhardtit. Zeit Krist 116:210–219. https://doi.org/10.1524/zkri.1961.116.16.210
[34] Bovio B, Locchi S (1982) Crystal structure of the orthorhombic basic copper nitrate, $Cu_2(OH)_3NO_3$. J Cryst Spectr Res 12:597–517. https://doi.org/10.1007/BF01160904
[35] Louër M, Grandjean D, Weigel D (1973) Etude structurale des hydroxynitrates de nickel et de zinc. II. Structure cristalline du nitrate basique de zinc $2Zn(OH)_2.Zn(NO_3)_2$. Acta Cryst B 29:1703–1707. https://doi.org/10.1107/S0567740873005297
[36] Eriksson L, Louër D, Werner PE (1989) Crystal structure determination and rietveld refinement of $Zn(OH)(NO_3)\cdot H_2O$. J Solid State Chem 81:9–20. https://doi.org/10.1016/0022-4596(89)90195-3
[37] Vilminot S, Richard-Plouet M, André G, Swierczynski D, Bourée-Vigneron F, Kurmoo M (2003) Hydrothermal synthesis in the system $Ni(OH)_2$-$NiSO_4$: nuclear and magnetic structures and magnetic properties of $Ni_3(OH)_2(SO_4)_2(H_2O)_2$. Inorg Chem 42:6859–6867. https://doi.org/10.1021/ic0345469
[38] Perchiazzi N (2006) Crystal structure determination and Rietveld refinement of rosasite and mcguinnessite. Z Kristallogr Suppl 23:505–510. https://doi.org/10.1524/9783486992526-084
[39] Girgsdies F, Behrens M (2012) On the structural relations of malachite. I. The rosasite and ludwigite structure families. Acta Cryst B68:107–117. https://doi.org/10.1107/S0108768112005125
[40] Gonzalez-Lopez J, Cockcroft JK, Fernandez-Gonzalez A, Jimenez A, Grau-Crespo R (2017) Crystal structure of cobalt hydroxide carbonate $Co_2CO_3(OH)_2$: density functional theory and X-ray diffraction investigation. Acta Cryst B73:868–873. https://doi.org/10.1107/S2052520617007983
[41] Arizaga CGC, Satyanarayana KG, Wypych F (2007) Layered hydroxide salts: synthesis, properties and potential applications. Solid State Ion 178:1143–1162. https://doi.org/10.1016/j.ssi.2007.04.016
[42] Nakagaki S, Machado GS, Stival JF, dos Santos EH, Machado Silva G, Wypych F (2021) Natural and synthetic layered hydroxide salts (LHS): recent advances and application perspectives emphasizing catalysis. Prog Solid State Chem 64:100335. https://doi.org/10.1016/j.progsolidstchem.2021.100335
[43] Arencibia N, Oestreicher V, Viva FA, Jobbagy M (2017) Nanotextured alpha Ni(II)–Co(II) hydroxides as supercapacitive active phases. RSC Adv 7:5595–5600. https://doi.org/10.1039/c6ra27839f
[44] Wei M, Li J, Chu W, Wang N (2019) Phase control of 2D binary hydroxides nanosheets via controlling-release strategy for enhanced oxygen evolution reaction and supercapacitor performances. J Energy Chem 8:26–33. https://doi.org/10.1016/j.jechem.2019.01.003
[45] Panda PK, Grigoriev A, Mishra YK, Ahuja R (2020) Progress in supercapacitors: roles of two dimensional nanotubular materials. Nanoscale Adv 2:70–108. https://doi.org/10.1039/c9na00307j
[46] Zhao Y, Wang Y, Huang J, Liu W, Hu J, Zheng J, Wu L (2023) Nickel carbonate Hydroxide-based core-triple-shelled nanofibers with ultrahigh specific capacity for flexible hybrid supercapacitors. J Colloid Interface Sci 630:444–451. https://doi.org/10.1016/j.jcis.2022.10.128
[47] Mackenzie M, Virnig M, Feather A (2006) The recovery of nickel from high-pressure acid leach solutions using mixed hydroxide product—LIX®84-INS technology. Miner Eng 19:1220–1233. https://doi.org/10.1016/j.mineng.2006.01.003
[48] Mubarok MZ, Lieberto J (2013) Precipitation of nickel hydroxide from simulated and atmospheric-leach solution of nickel laterite ore. Procedia Earth Planet Sci 6:457–464. https://doi.org/10.1016/j.proeps.2013.01.060
[49] Ma B, Yang W, Yang B, Wang C, Chen Y, Zhang Y (2015) Pilot-scale plant study on the innovative nitric acid pressure leaching technology for laterite ores. Hydrometallurgy 155:88–94. https://doi.org/10.1016/j.hydromet.2015.04.016
[50] Kurama H (2009) Treatment and recovery of nickel rich precipitate from plating plant waste. J Environ Eng Landsc Manag 17:212–218. https://doi.org/10.3846/1648-6897.2009.17.212-218
[51] Coman V, Robotin B, Ilea P (2013) Nickel recovery/removal from industrial wastes: a review. Resour Conserv Recycl 73:229–238. https://doi.org/10.1016/j.resconrec.2013.01.019
[52] Ge X, Gu CD, Wang XL, Tu JP (2015) Anomalous self-reduction of layered double hydroxide (LDH): from a-$Ni(OH)_2$ to hexagonal close packing (HCP) Ni/NiO by annealing without a reductant. Chem Commun 51:1004–1007. https://doi.org/10.1039/c4cc07767a
[53] Rajamathi M, Subbanna GM, Vishnu Kamath P (1997) On the existence of a nickel hydroxide phase which is neither α nor β. J Mater Chem 7:2293–2296. https://doi.org/10.1039/A700390K
[54] Méring J (1949) L'Interférence des Rayons X dans les systèmes à stratification désordonnée. Acta Cryst 2:371–377. https://doi.org/10.1107/S0365110X49000977
[55] Reynolds RC (1980) Interstratified clay minerals. In: Brindley GW, Brown G (eds) Crystal structures of clay minerals and their X-ray identification. Mineralogical Society, London, pp 249–304. https://doi.org/10.1180/mono-5.4
[56] Guggenheim S (2011) An overview of order/disorder in hydrous phyllosilicates. In: Brigatti MF, Mottana A (eds) Layered mineral structures and their application in advanced technologies.

European Mineraloical Union, Twickenham, pp 73–122. https://doi.org/10.1180/EMU-notes.11.2
[57] Moore D, Reynolds RC (1989) X-ray diffraction and identification and analysis of clay minerals. Oxford Universty Press, Oxford
[58] Lopez-Delgado A, Lopez-Andres S, Garcia-Martinez O, Millan P, Rojas RM (1987) Nickel basic salts as inorganic precursors in the production of nickel. J Mater Sci 22:2169–2174. https://doi.org/10.1007/BF01132955
[59] Rouba S, Rabu P, Ressouche E, Reganult LP, Drillon M (1996) Ferromagnetism in 1 d and 2d triangular nickel(II)-based compounds. J Magn Magn Mater 163:365–372. https://doi.org/10.1016/S0304-8853(96)00327-7
[60] Biswick T, Jones W, Pacula A, Serwicka E (2006) Synthesis, characterisation and anion exchange properties of copper, magnesium, zinc and nickel hydroxy nitrates. J Solid State Chem 179:49–55. https://doi.org/10.1016/j.jssc.2005.09.040
[61] Rajamathi M, Vishnu Kamath P, Seshadri R (2000) Polymorphism in nickel hydroxide: role of interstratification. J Mater Chem 10:503–506. https://doi.org/10.1039/A905651C
[62] Audemer A, Delahaye A, Farhi R, Sac-Epée N, Tarascon JM (1997) Electrochemical and Raman studies of beta-type nickel hydroxides $Ni_{1-x}Co_x(OH)_2$ electrode materials. J Electrochem Soc 144:2614–2620. https://doi.org/10.1149/1.1837873
[63] Ertaş FS, Kaş R, Ünal U, Birer O (2013) Sonochemical synthesis and electrochemical characterization of α-nickel hydroxide: precursor effects. J Solid State Electrochem 17:1455–1462. https://doi.org/10.1007/s10008-013-2017-3
[64] Wang YM, Zhao DD, Zhao YQ, Xu CL, Li HL (2012) Effect of electrodeposition temperature on the electrochemical performance of a $Ni(OH)_2$ electrode. RSC Adv 2:1074–1082. https://doi.org/10.1039/C1RA00613D
[65] Kovalenko V, Kotok V (2018) Comparative investigation of electrochemically synthesized (a+β) layered nickel hydroxide with mixture of α-$Ni(OH)_2$ and β-$Ni(OH)_2$. East-Eur J Enterp Technol 2:16–22. https://doi.org/10.15587/1729-4061.2018.125886
[66] Kotok V, Kovalenko V (2019) Influence of the carbonate ion on characteristics of electrochemically synthesized layered (α+β) nickel hydroxide. East-Eur J Enterp Technol 1:40–46. https://doi.org/10.15587/1729-4061.2019.155738
[67] Carlino S (1997) The intercalation of carboxylic acids into layered double hydroxides: a critical evaluation and review of the different methods. Solid State Ion 98:73–84. https://doi.org/10.1016/S0167-2738(96)00619-4
[68] Guillard D, Lewis AE (2001) Nickel carbonate precipitation in a fluidized-bed reactor. Ind Eng Chem Res 40:5564–5569. https://doi.org/10.1021/ie010312q
[69] Neimark AV, Ravikovitch PI (2001) Capillary condensation in MMS and pore structure characterization. Micropor Mesopor Mat 44–45:697–707. https://doi.org/10.1016/S1387-1811(01)00251-7
[70] Pandya KI, O'Grady WE, Corrigan DA, McBreen J, Hoffman RW (1990) Extended X-ray absorption fine structure investigations of nickel hydroxides. J Phys Chem 94:21–26. https://doi.org/10.1021/j100364a005
[71] Hall DS, Lockwood DJ, Poirier S, Bock C, MacDougall BR (2012) Raman and infrared spectroscopy of α and β phases of thin nickel hydroxide films electrochemically formed on nickel. J Phys Chem A 116:6771–6784. https://doi.org/10.1021/jp303546r
[72] Lanson B (2011) Modelling of X-ray diffraction profiles: Investigation of defective lamellar structure crystal chemistry. In: Brigatti MF, Mottana A (eds) Layered mineral structures and their application in advanced technologies. European Mineralogical Union, Twickenham, pp 151–202. https://doi.org/10.1180/EMU-notes.11.4
[73] Bailey SW (1982) Nomenclature for regular interstratification. Clay Miner 17:243–248. https://doi.org/10.1180/claymin.1982.017.2.09
[74] McEwen RS (1975) Crystallographic studies on nickel hydroxide and the higher nickel oxides. J Phys Chem 12:1782–1789. https://doi.org/10.1021/j100681a004
[75] Vaysse C, Guerlou-Demourgues L, Delmas C (2002) Thermal evolution of carbonate pillared layered hydroxides with (Ni, L) (L = Fe, Co) based slabs: grafting or nongrafting of carbonate anions? Inorg Chem 41:6905–6913. https://doi.org/10.1021/ic025542r
[76] Lavalley JC (1996) Infrared spectrometric studies of the surface basicity of metal oxides and zeolites using adsorbed probe molecules. Catal Today 27:377–401. https://doi.org/10.1016/0920-5861(95)00161-1
[77] Kloprogge JT, Wharton D, Hickey L, Frost RL (2002) Infrared and Raman study of interlayer anions CO_3^{2-}, NO_3^-, SO_4^{2-} and ClO^{4-} in Mg/Al hydrotalcite. Am Mineral 87:623–629. https://doi.org/10.2138/am-2002-5-604
[78] Kloprogge JT, Frost RL (1999) Fourier transform infrared and Raman spectroscopic study of the local structure of Mg-, Ni-, and Co-hydrotalcites. J Solid State Chem 146:506–515. https://doi.org/10.1006/jssc.1999.8413
[79] Kannan S, Narayanan A, Swamy CS (1996) Effect of composition on the physicochemical properties of nickel aluminium hydrotalcites. J Mater Sci 31:2353–2360. https://doi.org/10.1007/BF01152946
[80] Marappa S, Vishnu Kamath P (2015) Structure of the carbonate-intercalated layered double hydroxides: a reappraisal. Ind Eng Chem Res 54:11075–11079. https://doi.org/10.1021/acs.iecr.5b03207
[81] Wegrzyn A, Rafalska-Lasocha A, Majda D, Dziembaj R, Papp H (2010) The influence of mixed anionic composition of Mg–Al hydrotalcites on the thermal decomposition mechanism based on in situ study. J Therm Anal Calorim 99:443–457. https://doi.org/10.1007/s10973-009-0190-5
[82] Marappa S, Radha S, Vishnu Kamath P (2013) Nitrate-intercalated layered double hydroxides—structure model, order, and disorder. Eur J Inorg Chem 2013:2122–2128. https://doi.org/10.1002/ejic.201201405
[83] Bantignies JL, Deabate S, Righi A, Rols S, Hermet P, Sauvajol JL, Henn F (2008) New Insight into the vibrational behavior of nickel hydroxide and oxyhydroxide using inelastic neutron scattering, far/mid-infrared and raman spectroscopies. J Phys Chem C 112:2193–2201. https://doi.org/10.1021/jp075819e
[84] Rey F, Fornés V, Rojo JM (1992) Thermal decomposition of hydrotalcites. An infrared and nuclear magnetic resonance spectroscopic study. J Chem Soc Faraday Trans 88:2233–2238. https://doi.org/10.1039/FT9928802233
[85] Bae MS, Schwab JJ, Zhang Q, Hogrefe O, Demerjian KL, Weimer S, Rhoads K, Orsini D, Venkatachari P, Hopke PK (2007) Interference of organic signals in highly time resolved nitrate measurements by low mass resolution aerosol. J Geophys Res 112:D22305. https://doi.org/10.1029/2007JD008614
[86] Lebedeva O, Tichit D, Coq B (1999) Influence of the compensating anions of Ni/Al and Ni/Mg/Al layered double hydroxides on their activation under oxidising and reducing atmospheres. Appl Catal A Gen 183:61–71. https://doi.org/10.1016/S0926-860X(99)00039-3

[87] Stern KH (1972) High Temperature properties and decomposition of inorganic salts part 3. Nitrates and nitrites. J Phys Ref Data 1:747–772. https://doi.org/10.1063/1.3253104
[88] Kanezaki E (1998) Direct observation of a metastable solid phase of Mg/Al/CO3-layered double hydroxide by means of high temperature in situ powder XRD and DTA/TG. Inorg Chem 37:2588–2590. https://doi.org/10.1021/ic9715431
[89] Kanezaki E (1998) Thermal behavior of the hydrotalcite-like layered structure of Mg and Al-layered double hydroxides with interlayer carbonate by means of in situ powder HTXRD and DTA/TG. Solid State Ionics 106:279–284. https://doi.org/10.1016/S0167-2738(97)00494-3
[90] Costa DG, Rocha AB, Souza WF, Shirley S, Chiaro X, Leitão AA (2012) Ab initio study of reaction pathways related to initial steps of thermal decomposition of the layered double hydroxide compounds. J Phys Chem C 116:13679–13687. https://doi.org/10.1021/jp303529y
[91] Rhamdhani MA, Jak E, Hayes PC (2008) Basic nickel carbonate: Part I. microstructure and phase changes during oxidation and reduction processes. Metal Mater Trans B 39:218–233. https://doi.org/10.1007/s11663-007-9124-4
[92] Bera P, Rajamathi M, Hegde MS, Kamath VP (2000) Thermal behaviour of hydroxides, hydroxysalts and hydrotalcites. Bull Mater Sci 23:141–145. https://doi.org/10.1007/BF02706556
[93] Cabanas-Polo S, Ferrari B, Sanchez-Herencia AJ (2014) Colloidal stability of $Ni(OH)_2$ in water and its dispersion into a ceramic matrix from the reaction media to obtain Ni/Al_2O_3 materials. Bol Soc Esp Ceram Vidr 53:265–274. https://doi.org/10.3989/cyv.322014
[94] Bénard P, Auffredic JP, Louër DL (1994) A study of the thermal decomposition of ammine zinc hydroxide nitrates. Thermochim Acta 232:65–76. https://doi.org/10.1016/0040-6031(94)80046-4
[95] Chmielarz L, Kustrowski P, Rafalska-Lasocha A, Dziembaj R (2003) Influence of Cu, Co and Ni cations incorporated in brucite-type layers on thermal behaviour of hydrotalcites and reducibility of the derived mixed oxide systems. Thermochim Acta 395:225–236. https://doi.org/10.1016/S0040-6031(02)00214-9
[96] Tichit D, Medina F, Coq B, Dutartre R (1997) Activation under oxidizing and reducing atmospheres of Ni-containing layered double hydroxides. Appl Catal A Gen 159:241–258. https://doi.org/10.1016/S0926-860X(97)00085-9
[97] Escalona Platero E, Fubini B, Zecchina (1987) Nitric oxide adsorption on NiO: an infrared and calorimetric study. Surf Sci 179:404–424. https://doi.org/10.1016/0039-6028(87)90066-5
[98] Brockner W, Ehrhardt C, Gjikaj M (2007) Thermal decomposition of nickel nitrate hexahydrate, $Ni(NO_3)_2{\cdot}6H_2O$, in comparison to $Co(NO_3)_2{\cdot}6H_2O$ and $Ca(NO_3)_2{\cdot}4H_2O$. Thermochim Acta 456:64–68. https://doi.org/10.1016/j.tca.2007.01.031
[99] Fingerle M, Tengeler S, Calvet W, Jaegermann W, Mayer T (2020) Sputtered nickel oxide thin films on n-Si(100)/SiO2 surfaces for photo-electrochemical oxygen evolution reaction (OER): impact of deposition temperature on OER performance and on composition before and after OER. J Electrochem Soc 167:136514. https://doi.org/10.1149/1945-7111/abbcdf
[100] Wolfart F, Dubal DP, Vidotti M, Gomez-Romero P (2016) Hybrid core–shell nanostructured electrodes made of polypyrrole nanotubes coated with $Ni(OH)_2$ nanoflakes for high energy-density supercapacitors. RSC Adv 6:15062–15070. https://doi.org/10.1039/c5ra23671a
[101] Guo Y, Wei Y, Li H, Zha T (2017) Layer structured materials for advanced energy storage and conversion. Small 13:1701649. https://doi.org/10.1002/smll.201701649
[102] Brisse A-L, Stevens P, Toussaint G, Crosnier O, Brousse Y (2018) $Ni(OH)_2$ and NiO based composites: battery type electrode materials for hybrid supercapacitor devices. Materials 11:1178. https://doi.org/10.3390/ma11071178
[103] Scala-Benuzzi ML, Fernández SN, Giménez G, Ybarra G, Soler-Illia GJAA (2023) Ordered mesoporous electrodes for sensing applications. ACS Omega 8:24128–32415. https://doi.org/10.1021/acsomega.3c02013
[104] Thommes M, Kaneko K, Neimark AV, Olivier JP, Rodriguez-Reinoso F, Rouquerol J, Sing KSW (2015) Physisorption of gases, with special reference to the evaluation of surface area and pore size distribution (IUPAC technical report). Pure Appl Chem 87:1051–1069. https://doi.org/10.1515/pac-2014-1117
[105] Gash AE, Satcher JHJ, Simpson RL (2004) Monolithic nickel(II)-based aerogels using an organic epoxide: the importance of the counterion. J Non-Cryst Solids 350:145–151. https://doi.org/10.1016/j.jnoncrysol.2004.06.030
[106] Yi X, Sun H, Robertson N, Kirk C (2021) Nanoflower Ni(OH)2 grown in situ on Ni foam for high-performance supercapacitor electrode materials. Sustain Energy Fuels 5:5236–5246. https://doi.org/10.1039/d1se01036k
[107] Trens P, Tanchoux N, Galarneau A, Brunel D, Fubini B, Garrone E, Fajula F, Di Renzo F (2005) A macrothermodynamic approach to the limit of reversible capillary condensation. Langmuir 21:8560–8564. https://doi.org/10.1021/la0507838
[108] Aguilera L, Leyet Y, Padrón-Hernández E, Passos RR, Pocrifka LA (2018) Understanding electrochemical performance of $Ni(OH)_2$ films: a study contributions to energy storage. J Solid State Electrochem 22:1621–1628. https://doi.org/10.1007/s10008-017-3737-6
[109] Huang L-F, Hutchison MJ, Santucci RJ, Scully JR, Rondinelli JM (2017) Improved electrochemical phase diagrams from theory and experiment: the Ni−water system and its complex compounds. J Phys Chem C 121:9782–9789. https://doi.org/10.1021/acs.jpcc.7b02771
[110] Kettaf S, Guellati O, Harat A, Kennaz H, Momodu D, Dangbegnon J, Manyal N, Guerioune M (2019) Electrochemical measurements of synthesized nanostructured β-$Ni(OH)_2$ using hydrothermal process and activated carbon based nanoelectroactive materials. SN Appl Sci 1:34. https://doi.org/10.1007/s42452-018-0038-3
[111] Delahaye-Vidal A, Figlarz M (1987) Textural and structural studies on nickel hydroxide electrodes. II. Turbostratic nickel (II) hydroxide submitted to electrochemical redox cycling. J Applied Electrochem 17:589–599. https://doi.org/10.1007/BF01084134
[112] Trafela Š, Zavašnik J, Šturm S, Rožman KŽ (2020) Controllable voltammetric formation of a structurally disordered NiOOH/$Ni(OH)_2$ redox pair on Ni-nanowire electrodes for enhanced electrocatalytic formaldehyde oxidation. Electrochim Acta 362:137180. https://doi.org/10.1016/j.electacta.2020.137180
[113] Zhu G, Xi C, Shen M, Bao C, Zhu J (2014) Nanosheet-based hierarchical Ni2(CO3)(OH)2 microspheres with weak crystallinity for high-performance supercapacitor. ACS Appl Mater Interfaces 6:17208–17214. https://doi.org/10.1021/am505056d
[114] Lee JW, Ko JM, Kim JD (2011) Hierarchical microspheres based on α-Ni(OH)2 nanosheets intercalated with different anions: synthesis, anion exchange, and effect of intercalated anions on electrochemical capacitance. J Phys Chem C 115:19445–19454. https://doi.org/10.1021/jp206379h